



HAL
open science

Quantum Capacitance through Molecular Infiltration of 7,7,8,8-Tetracyanoquinodimethane in Metal–Organic Framework/Covalent Organic Framework Hybrids

Haijun Peng, Senhe Huang, Diana Tranca, Fanny Richard, Walid Baaziz,
Xiaodong Zhuang, Paolo Samorì, Artur Ciesielski

► **To cite this version:**

Haijun Peng, Senhe Huang, Diana Tranca, Fanny Richard, Walid Baaziz, et al.. Quantum Capacitance through Molecular Infiltration of 7,7,8,8-Tetracyanoquinodimethane in Metal–Organic Framework/Covalent Organic Framework Hybrids. *ACS Nano*, 2021, 15 (11), pp.18580-18589. 10.1021/acsnano.1c09146 . hal-03450331

HAL Id: hal-03450331

<https://hal.science/hal-03450331>

Submitted on 25 Nov 2021

HAL is a multi-disciplinary open access archive for the deposit and dissemination of scientific research documents, whether they are published or not. The documents may come from teaching and research institutions in France or abroad, or from public or private research centers.

L'archive ouverte pluridisciplinaire **HAL**, est destinée au dépôt et à la diffusion de documents scientifiques de niveau recherche, publiés ou non, émanant des établissements d'enseignement et de recherche français ou étrangers, des laboratoires publics ou privés.

Quantum Capacitance through Molecular Infiltration of 7,7,8,8-Tetracyanoquinodimethane in Metal–Organic Framework / Covalent Organic Framework Hybrids

*Haijun Peng,[†] Senhe Huang,[‡] Diana Tranca,[‡] Fanny Richard,[†] Walid Baaziz,[§] Xiaodong
Zhuang,[‡] Paolo Samorì*[†] and Artur Ciesielski*[†]*

[†]Université de Strasbourg, CNRS, Institut de Science et d'Ingénierie Supramoléculaires, 8 allée
Gaspard Monge, 67000 Strasbourg, France

[‡]The Soft2D Lab, State Key Laboratory of Metal Matrix Composites, Shanghai Key Laboratory
of Electrical Insulation and Thermal Ageing, School of Chemistry and Chemical Engineering,
Shanghai Jiao Tong University, 200240, Shanghai, China

[§]Université de Strasbourg, CNRS, IPCMS UMR 7504, 23 rue du Loess, 67034 Strasbourg
(France)

Abstract: Metal–organic frameworks (MOFs) and covalent organic frameworks (COFs) have been extensively investigated during the last two decades. More recently, a family of hybrid materials, *i.e.*, MOF@COF has emerged as particularly appealing for gas separation and storage, catalysis, sensing and drug delivery. MOF@COF hybrids combine the unique characteristics of both MOF and COF components and exhibit peculiar properties including high porosity and large surface area. In this work, we show that the infiltration of redox-active 7,7,8,8-tetracyanoquinodimethane (TCNQ) molecules into the pores of MOF@COF greatly improves the characteristics of the latter thereby attaining high-performance in energy storage devices. Density functional theory (DFT) calculations were employed to guide the design of a MOF@COF-TCNQ hybrid with the TCNQ functional units incorporated in the pores of MOF@COF. To demonstrate potential application of our hybrids, the as-synthesized MOF@COF-TCNQ hybrid has been employed as active material in supercapacitors. Electrochemical energy storage analysis revealed outstanding supercapacitor performance as evidenced by a specific areal capacitance of 78.36 mF cm⁻² and a high stack volumetric energy density of 4.46 F cm⁻³, with a capacitance retention of 86.4% after 2000 cycles completed at 0.2 A cm⁻². DFT calculations result strongly indicate that the high capacitance of MOF@COF-TCNQ has a quantum capacitance origin. Our liquid-phase infiltration protocol of MOF@COF hybrids with redox-active molecules represents a efficacious approach to design functional porous hybrids.

KEYWORDS: molecular-infiltration, metal-organic frameworks, covalent organic frameworks, quantum-capacitance, supercapacitors

The ever-increasing energy demands have pushed worldwide research efforts towards the development of renewable energy technologies.¹ Supercapacitors are extremely powerful energy storage devices that combine an eco-friendly nature, cost-effectiveness, high durability, high power, and moderate energy density.^{2,3} During the last few years, substantial attention has been paid to the synthesis of different materials for supercapacitor electrodes,^{4,8} mainly relying on pseudo-capacitance and electrical double layer capacitance (EDLC). Nevertheless, quantum capacitance, being one of the physical mechanisms giving rise to interfacial capacitance, is little exploited and not yet fully understood. Xia *et al.* and S. Ilani *et al.* reported that the quantum capacitance of graphene and carbon nanotubes may be the origin of the increased interfacial capacitance in particular carbon-based devices.^{9,10} Subsequently, Zhang *et al.*¹¹ and Song *et al.*¹² further investigated this concept by introducing nitrogen or oxygen-containing (hydroxyl and epoxy) groups in graphene, which was found to be advantageous for the enhancement of the quantum capacitance. Besides the aforementioned examples, the quantum capacitance mechanism has not been explored in materials employed as supercapacitor electrodes.

In the last two decades, the tremendous effort devoted to the generation of highly porous materials has laid the groundwork for functional systems, which find their application in our daily life. Among such emerging porous metal–organic frameworks (MOFs) and covalent organic frameworks (COFs) crystalline architectures gained overgrowing interest *since* their properties can be tailored also in large-scale processes. On the one hand, MOFs are typically assembled through the non-covalent interactions between metallic species and multidentate ligands.¹³ On the other hand, COFs are thoroughly formed by covalent bonds, such as imines, nitroborates, boronyls, and C=C.¹⁴ Notably, MOFs and COFs are considered as propitious electrode materials for leading edge energy storage devices due to their crystalline porous structures featuring high specific surface

area, and the presence of numerous functional redox-active sites.¹⁵⁻²⁰ Nonetheless, traditional MOFs and COFs suffer from low electrical conductivities, resulting from the insulating nature of the organic ligands used for their assembly, and π -d orbital overlap between organic ligands metal ions, which limits their electro-chemical performance in energy storage application.²¹ Therefore, the porous structure in MOFs and redox-active sites in COFs cannot be fully exploited, jeopardizing their practical applications in supercapacitors. A viable solution to enhance MOFs and COFs capacitance as supercapacitor electrode consists in the incorporation of conductive materials like carbon nanotubes,²² graphene,^{23,24} and conducting polymers^{25,26} in their porous structure.

Lately, MOFs@COFs hybrid structures containing traits of both MOFs and COFs have stand out as a family of porous hybrids exhibiting advantages of individual components, to enable to harvest the performance in gas separation,²⁷ (photo)catalysis,^{28,29} sensors,³⁰ bacterial inhibition³¹ and lithium-ion batteries.³² Typically, MOFs@COFs are generated through the condensation of amine-functionalized MOFs and amine-based COFs, yielding in imine formation at the interface between the two components. The number of reports dealing with MOFs@COFs hybrid porous nanomaterials has rapidly increased, most of which target taking full advantage of the properties that go beyond the simple sum of those exhibited by the pristine MOFs and COFs. For instance, Fu *et al.* introduced the COF-300@ZIF-8 hybrid that was employed as membrane material and displayed increased separation selectivity towards H₂/CO₂ gas mixtures when compared with membranes generated from the single MOF or COF components.²⁷ Subsequently, various MOFs@COFs including NH₂-MIL-68-MOF@COF,³³ NH₂-UIO-66@COF-TpPa,²⁸ NH₂-MIL-125@COF-LZU1,²⁹ and UIO-66-NH₂@COF-TAPB-BTCA were successfully explored in (photo)catalysis. Nevertheless, excluding the specific case of Mn-MOF@COF³² described by Wang *et*

al., and aza-MOF@COF-LZU1 reported by our group, the utilization of MOFs@COFs hybrids remains to a great extent uncharted in energy storage.

In order to unravel the potential of MOFs@COFs in energy storage application, an alternative approach consists of the use of the MOF or COF pores as platforms for modulating the electrical transport properties. Since Talin *et al.* described the example of tuning the electrical conductivity in MOFs *via* the incorporation of redox-active 7,7,8,8-tetracyanoquinodimethane (TCNQ) within the pores of Cu_3BTC_2 (also called HKUST-1; BTC= 1,3,5-benzenetricarboxylate),²¹ a series of structural and computational studies were undertaken to explore the influence of the electron-acceptor guest TCNQ on the electron-donor host MOFs or COFs.³⁴⁻³⁸ Noteworthy, Feng *et al.* have demonstrated the electronic doping of MOF with TCNQ by employing $\text{TCNQ}@Cu_3(\text{BTC})_2$ as an active material micro-supercapacitors.³⁹ Hitherto, the infiltration of TCNQ into MOFs@COFs and their application in energy storage is still unexplored. We envision that the infiltration of TCNQ into the pores of MOFs@COFs hybrid could harness their performance as supercapacitor electrodes.

Here we report a MOF@COF-TCNQ hybrid formed through a liquid-phase infiltration of TCNQ into the MOF@COF pore channels. As a proof-of-concept application, MOF@COF-TCNQ hybrid has been employed as a supercapacitor electrode, which exhibited a high specific areal capacitance of 78.36 mF cm^{-2} accompanied by a high stack capacitance of 4.46 F cm^{-3} , outperforming the majority of state-of-the-art MOFs@COFs hybrids. Moreover, by combining the experimental results with DFT calculations we introduce the concept of quantum capacitance to MOF@COF hybrids.

RESULTS AND DISCUSSION

Structural and Morphological Characterization. The general strategy leading to the production of MOF@COF-TCNQ has been portrayed in Figure 1. MOF-UIO-66-NH₂ ([Zr₆O₄(OH)₄-(ATA)₁₂] (ATA:2-aminoterephthalate)), was synthesized according to the protocol reported in Ref.,⁴⁰ with the slight alteration being the use of surfactant (polyvinylpyrrolidone (PVP)), to enhance the dispersibility of MOF-UIO-66-NH₂ which enables successful nucleation of enamine-linked COF on its surface (see the Methods for the experimental details). An enamine-linked COF-TpPa⁴¹ has been chosen to generate the core-shell hybrid since it exhibits high chemical (acid/base) stability and good electrochemical properties that were previously explored in energy storage,³⁴ batteries, and supercapacitor electrodes.⁴³⁻⁴⁵ The MOF@COF-TCNQ hybrid material was generated through on-surface condensation of the MOF-UIO-66-NH₂ with 1,3,5-triformylphloroglucinol (Tp), which yields in MOF-UIO-66-NH₂ (Tp). Subsequently, the COF shell was generated on MOF-UIO-66-NH₂ (Tp) *via* the condensation with *p*-phenylenediamine. Lastly, liquid-phase infiltration of electron acceptors TCNQ yielding the MOF@COF-TCNQ hybrids was employed.

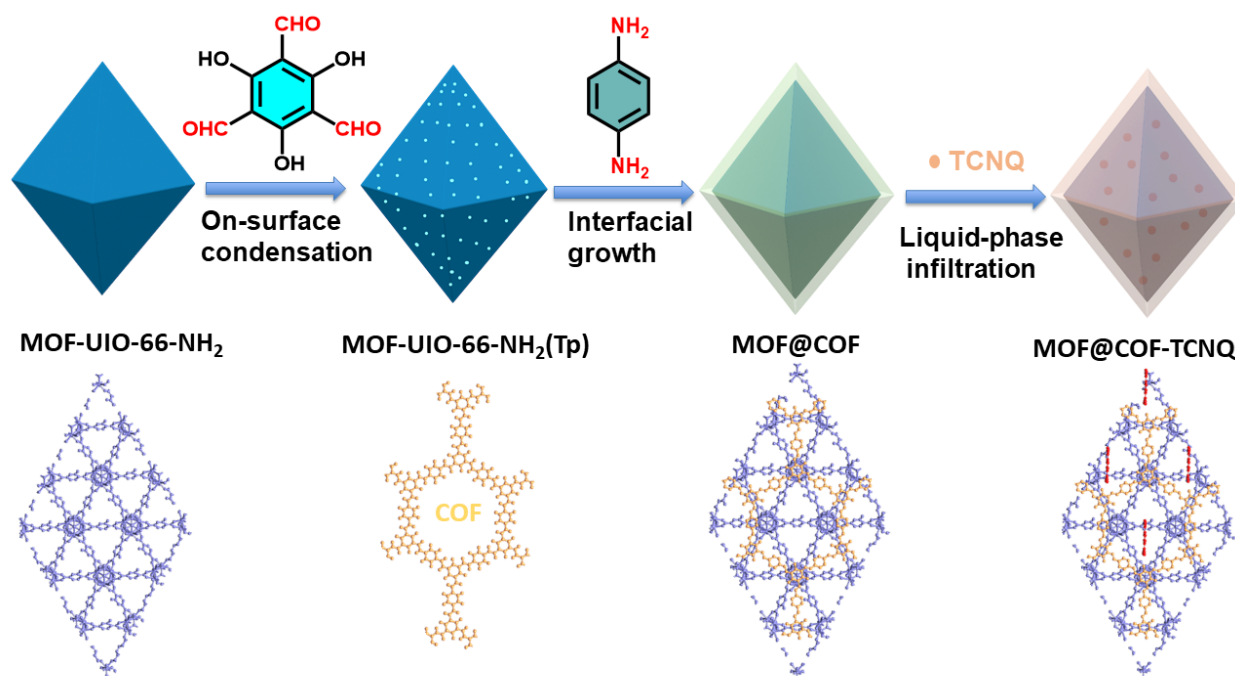


Figure 1. The schematic of a synthesis route for MOF@COF-TCNQ hybrids.

The structures of the investigated hybrids were firstly examined with Fourier transform infrared (FTIR) spectroscopy and powder X-ray diffraction (PXRD). The patterns of the MOF-UIO-66-NH₂ (Figure S1 and S2) resulted to be in good accordance with those previously reported.²⁸ The growth of COF-TpPa on the surface of MOF-UIO-66-NH₂ and subsequent liquid-phase infiltration with TCNQ yielding MOF@COF-TCNQ were inspected by various analytical techniques. The existence of a diffraction peak at 4.7°, originating from the (1 0 0) plane of COF-TpPa (Figure 2a), highlights the formation of COF-TpPa on the MOF@COF.⁴¹ Note that the PXRD patterns of the as-synthesized MOF@COF after TCNQ infiltration remained unchanged, which proves that the crystalline structure of MOF@COF is unaffected throughout the infiltration process. Conversely, major differences in the PXRD patterns of MOF-UIO-66-NH₂ were observed after embedding the TCNQ (Figure S3) which also yields in a major color change from light yellow to dark green (Figure 2a). Such observations confirmed the superior stability of MOF@COF structure

over MOF-UIO-66-NH₂ during the infiltration process. The comparison of FTIR spectra of MOF@COF-TCNQ with MOF-UIO-66-NH₂ and MOF@COF evidenced the existence of a band at about 2212 cm⁻¹, that is ascribed to the C≡N stretch mode of TCNQ (Figure S4).⁴⁶ The UV-vis absorption spectroscopy of MOF@COF-TCNQ compared with MOF-UIO-66-NH₂ and MOF@COF showed a broad red-shift, demonstrating that the infiltrated TCNQ is effective in imparting π -conjugation over the MOF@COF skeleton than the pristine MOF-UIO-66-NH₂ (Figure 2c).⁴⁷

X-ray photoelectron spectroscopy (XPS) has been employed to shed light on the nature and the electronic states of the N atoms in MOF@COF-TCNQ after TCNQ infiltration. The examination of N 1s spectra of MOF-UIO-66-NH₂ provided evidence for the existence of a feature at 399.5 eV which can be ascribed to primary amines (-NH₂). The peak appearing at 401.6 eV can be ascribed to -NH moieties of the organic linkers in pure UIO-66-NH₂.^{29,48} MOF@COF N 1s spectra displayed two new peaks at 400.08 eV and 403.34 eV, indicating the formation of enamine (C-NH-C) bond and π - π^* satellite peak, being in line with previous reports.⁴⁹ Upon post-synthetic modification of infiltrating TCNQ, a fraction of N1s appeared at higher binding energies, *i.e.* 400.4 eV (Figure 2f), corresponding to the nitrile (-C≡N) in TCNQ moieties.⁵⁰ High-resolution C1s spectra depicted in Figure S5 also display a peak of -C≡N groups,⁵¹ and serves as a further indication for the presence of TCNQ in the doped MOF@COF.

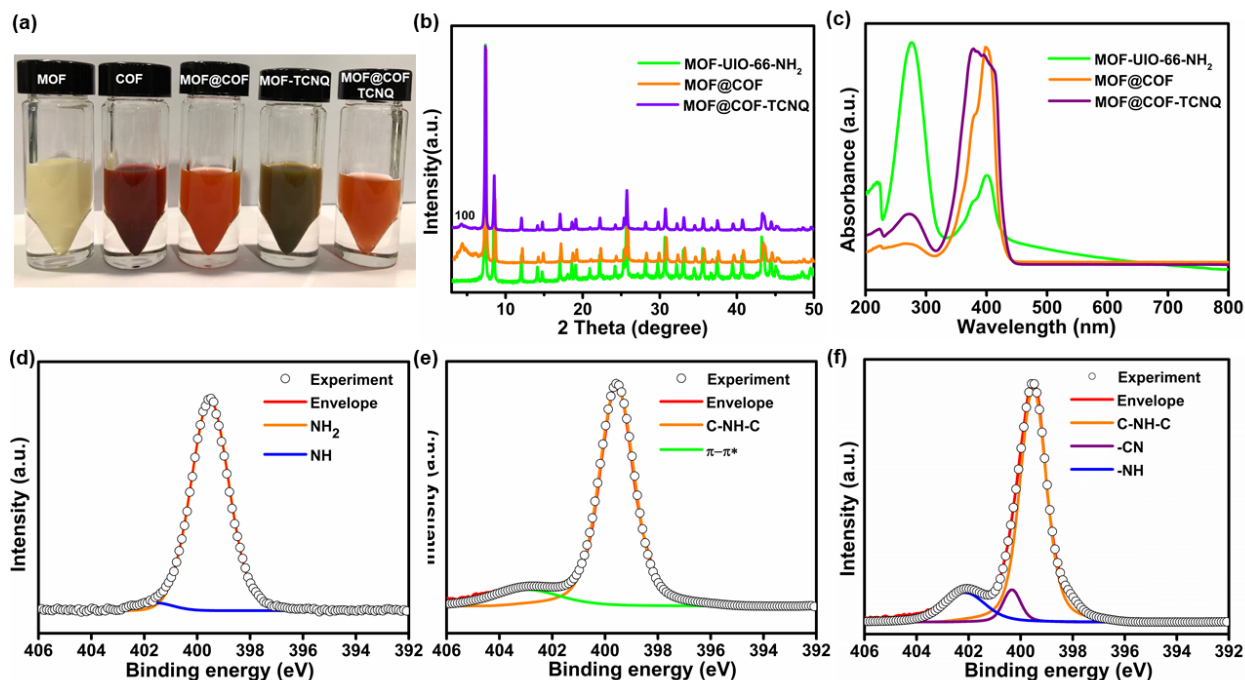


Figure 2. MOF-UIO-66-NH₂, MOF@COF, and MOF@COF-TCNQ. (a) Optical image of all the synthesized materials. (b) XRD patterns of MOF-UIO-66-NH₂, MOF@COF, and MOF@COF-TCNQ. (c) UV-vis absorption spectra of MOF-UIO-66-NH₂, MOF@COF, and MOF@COF-TCNQ. (d-f) XPS spectra of MOF-UIO-66-NH₂, MOF@COF, and MOF@COF-TCNQ, respectively.

The chemical composition of MOF@COF and the content of the infiltrated TCNQ were further investigated by means of matrix-assisted laser desorption/ionization-time-of-flight (MALDI-TOF) mass spectra in combination with thermogravimetric analysis (TGA) and differential scanning calorimetry (DSC). Figure S6 displays the MALDI-TOF mass spectra which does not show any chemical changes that could be expected from the infiltration of TCNQ into MOF@COF. The TGA and DSC spectra depicted in Figure S7 reveal ca. 19% mass loss lower than 150 °C which can be attributed to the elimination of the solvent molecules present inside the pores of pristine MOF-UIO-66-NH₂. After coating of MOF-UIO-66-NH₂ with COF and subsequent infiltration with

TCNQ, the amounts of solvent molecules were found to be much lower and amounted to ca. 11% and ca. 8% for MOF@COF and MOF@COF-TCNQ, respectively. The main mass loss observed in the temperature range 150 and 700 °C can be attributed to the degradation of the framework and thermal decomposition of TCNQ (280-500 °C),⁵² which is determined to be ca. 42 %, 53 %, and 59% for MOF-UIO-66-NH₂, MOF@COF, and MOF@COF-TCNQ, respectively. Based on such observations, we could roughly estimate the content of TCNQ in MOF@COF-TCNQ, which amounts to ca. 6%. N₂ adsorption and desorption isotherms experiments were performed to quantify the porosity, and all isotherms were found to follow the type IV curve.⁵³ Not surprisingly, a reduction of Brunauer-Emmett-Teller (BET) surface areas is monitored, from 526 m² g⁻¹ for MOF@COF to 265 m² g⁻¹ for MOF@COF-TCNQ, compared with pristine MOF-UIO-66-NH₂ about 585 m² g⁻¹ (Figure S8). Pore size distribution quantification based on Barrett-Joyner-Halenda (BJH) studies revealed an increase of pore sizes from 0.6 nm to 1.6 nm upon growing COF layer on MOF-UIO-66-NH₂ and a slight reduction to ca. 0.9 nm after infiltrating of TCNQ (Figure S9), which provides further confirmation for the inclusion of the TCNQ molecules inside the MOF@COF framework.

The morphologies of all hybrid materials have been investigated with field-emission scanning electron microscopy (FE-SEM) and high-resolution transmission electron microscopy (HR-TEM). MOF-UIO-66-NH₂ octahedral particles possessing a mean diameter of ~200 nm are displayed in Figure 4a. When their surface is modified with COF, the particles maintain the overall morphology, yet, their diameter increases by ~20 nm as depicted in Figure 3d. Notably, upon TCNQ infiltration, the surface of MOF@COF-TCNQ particles exhibits increased roughness and a ~10 nm enhancement of the particles' diameter (~230 nm, Figure 3g). The High Resolution - Transmission Electron Microscopy images of MOF@COF particles shown in Figure 3f reveal the

existence of a ~ 20 nm thick layer of COF-TpPa at the edge of pristine MOF-UIO-66-NH₂. Noteworthy, the TCNQ infiltration, the MOF@COF-TCNQ particles exhibit apparent defects in the COF-TpPa lattice layer in Figure 3i, which can be attributed to the added TCNQ molecules. By combining the results of HR-TEM and pore size distribution, we can further confirm the existence of TCNQ molecules within the MOF@COF pores.

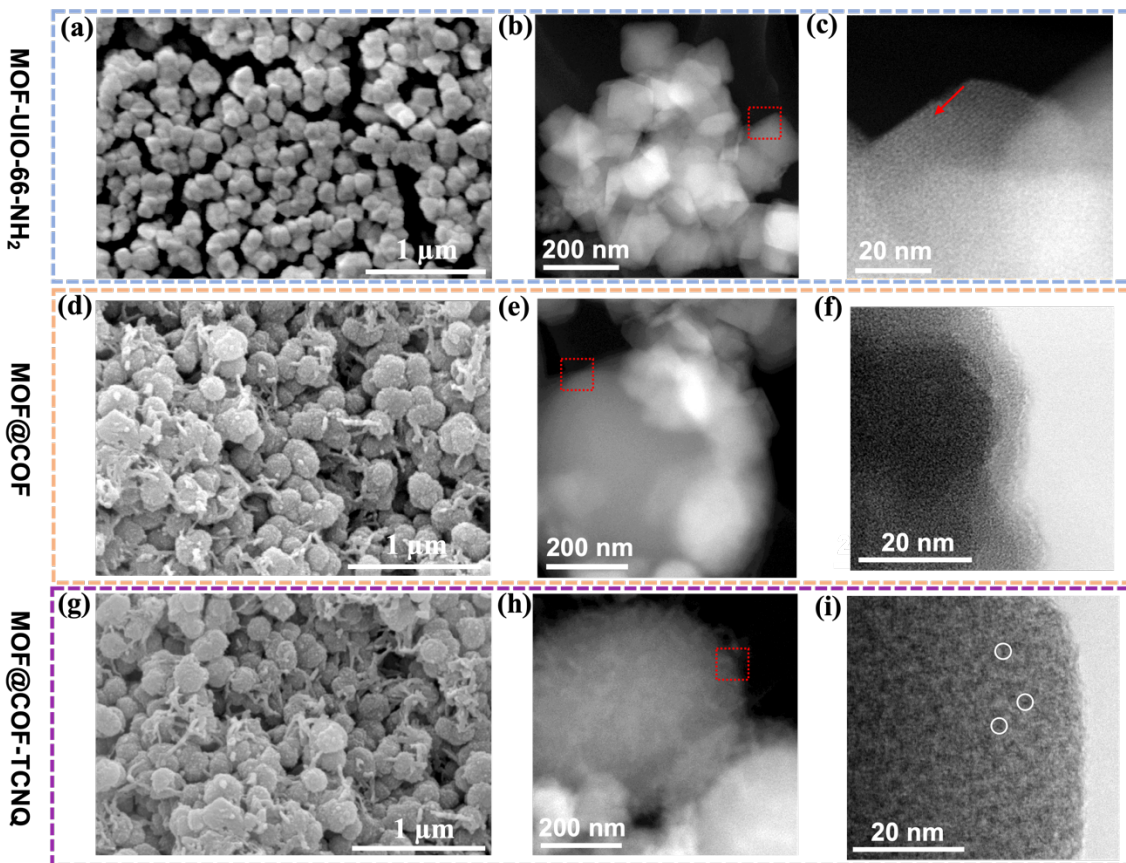


Figure 3. The SEM (left) images, TEM (middle) and HR-TEM (right) of (a)-(c) of MOF-UIO-66-NH₂, (d)-(f) MOF@COF and (g)-(i) MOF@COF-TCNQ.

Electrochemical Properties. All hybrid materials were subsequently employed as electrodes in both two- and three-electrode symmetric solid-state supercapacitors (as detailed in Methods and Figure S10). Hybrid materials as well as neat components have been employed as electrodes and

tested in a three-electrode system in 1M solution of H₂SO₄. Cyclic voltammograms (CV) were recorded in a 10 to 1000 mV s⁻¹ scan range from with the potential values swept in a range of the cut-off values (0≤E≤0.8). Such protocol allows for the capacitance performance, where all the device components, *i.e.*, the substrate, the separator and a pair of active materials are taken into account⁵⁴ (Figure 4 a-c). The CV voltammograms of the MOF@COF-based electrode exhibit an evident pair of redox peaks compared with MOF-UIO-66-NH₂, indicating the existence of a redox reaction in MOF@COF and revealing that the obtained capacitance consists of both pseudo-capacitance and electric double-layer capacitance. The position of the redox peak did not shift when the scanning rate was increased, indicating that electron transfer between electrolyte and the MOF@COF electrode is rapid and reversible.⁵⁵ MOF@COF-TCNQ based electrodes displayed a more rectangular-like shape and are characterized by greater current values when compared to MOF@COF, substantiating the enhanced electrochemical capacitance and the stability of the material.^{56,57} Specific capacitance estimated from the CV curves recorded at variable scan rates and charge/discharge profiles in Figure S10-12 in the Supporting Information was employed to evaluate the charge storage capacitance at different current densities of the supercapacitors. The areal capacitance of MOF-UIO-66-NH₂, MOF@COF, and MOF@COF-TCNQ were quantified as 8.21, 54.02, and 78.36 mF cm⁻², respectively (Figure 4d). The related stack capacitance was estimated as 0.46, 3.12, and 4.46 F cm⁻³, respectively. The measured capacitance of MOF@COF-TCNQ is a factor of two greater than the one of the neat MOF-UIO-66-NH₂ and MOF@COF. It is worth noting that such capacitance is also higher than those of activated carbon, graphene and considerably greater than other previously investigated systems (*i.e.* MOFs and COFs based) (Supporting Information, Table S1). Moreover, the MOF@COF-TCNQ cell displays good cycling stability with capacitance retention of 86.4% when benchmarked with MOF-UIO-66-NH₂(64.5%)

and MOF@COF (76.2%) after 2000 cycles executed with a current density of 0.2 A cm⁻² (Figure 4e). The electrochemical kinetics of all hybrid materials have been investigated by exploiting the procedure proposed by Dunn and co-workers.⁵⁸ The relation of the peak current I and scan rate v from CV complies with the equation $i=av^b$. The average value of b for MOF@COF-TCNQ compared with MOF@COF and MOF-UIO-66-NH₂ are near to 1 (Figure S14), indicating a predominantly capacitor-controlled process and denoting simple reaction kinetics. The excellent capacitance of MOF@COF-TCNQ can be ascribed to the uniform pores that facilitate the diffusion of ions and the redox behavior of doped β -keto-enamine linked COF on MOF which can provide extra pseudocapacitance. On the other hand, the highly crystalline structure and well-defined porous structure forming channels allow fast transport of ions, and the redox-active TCNQs embedded in the framework of MOF@COF ensure the fast electron transfer during the charge-discharge process in the supercapacitor devices.

Electrochemical impedance spectroscopy (EIS) characterizations were carried out in order to estimate the internal resistance in the process of charge transfer within the samples. As depicted in Figure 4f, a fairly minor semicircle observed within the high-frequency region signifies the foremost supercapacitor's resistive nature, which consists of electrode/electrolyte/current collector. The initial part of the semicircle line can be ascribed to the resistance (R_s) of the electrolyte in contact with the current collector and the electrode. The final part of the semicircle line is governed by the internal resistance (R_p) of the electrode materials. The R_p - R_s semicircle diameter links to the equivalent series resistance (ESR)⁵⁹ which amount to 212.6, 185.2, and 74.5 Ω cm⁻¹ for MOF-UIO-66-NH₂, MOF@COF, and MOF@COF-TCNQ, respectively. The ESR findings endorse our claims that the TCNQ infiltration into the MOF@COF yields enhanced electrical conductivity of the latter. On the other hand, from the EIS curves it is possible to

calculate the Warburg resistance (Z_w), with Z_w characterizing the diffusion resistance of electrolyte ions through the electrode, and its value mainly depends on the straight-line slope in the low-frequency region. An enhanced slope was observed for the linear part of the EIS curve of MOF@COF-TCNQ when benchmarked to that of neat MOF-UIO-66-NH₂ and MOF@COF, implying amplified ion and electron transports yielding improved capacitance. To broaden our assessment of the TCNQ doping, symmetrical supercapacitors consisting of a two-electrodes were built by using MOF-UIO-66-NH₂, MOF@COF, and MOF@COF-TCNQ as the electrodes and an aprotic electrolyte 1M tetraethylammonium tetrafluoroborate (TEABF₄) in acetonitrile (AN) as electrolyte. The devices exhibit similar capacitance increases for TCNQ-doped MOF@COF-TCNQ electrodes when examined in aprotic electrolytes (Figure S15). These findings encouraged us to unveil the mechanism(s) for the capacitance enhancement resulting from the TCNQ doping of MOF@COF. Noteworthy, to explore the content of TCNQ for the contribution of supercapacitors performance, we mixed the TCNQ with MOF@COF to construct supercapacitor devices, and the devices were short-circuited because the mixed TCNQ moieties can cross over the separator into the electrolyte.

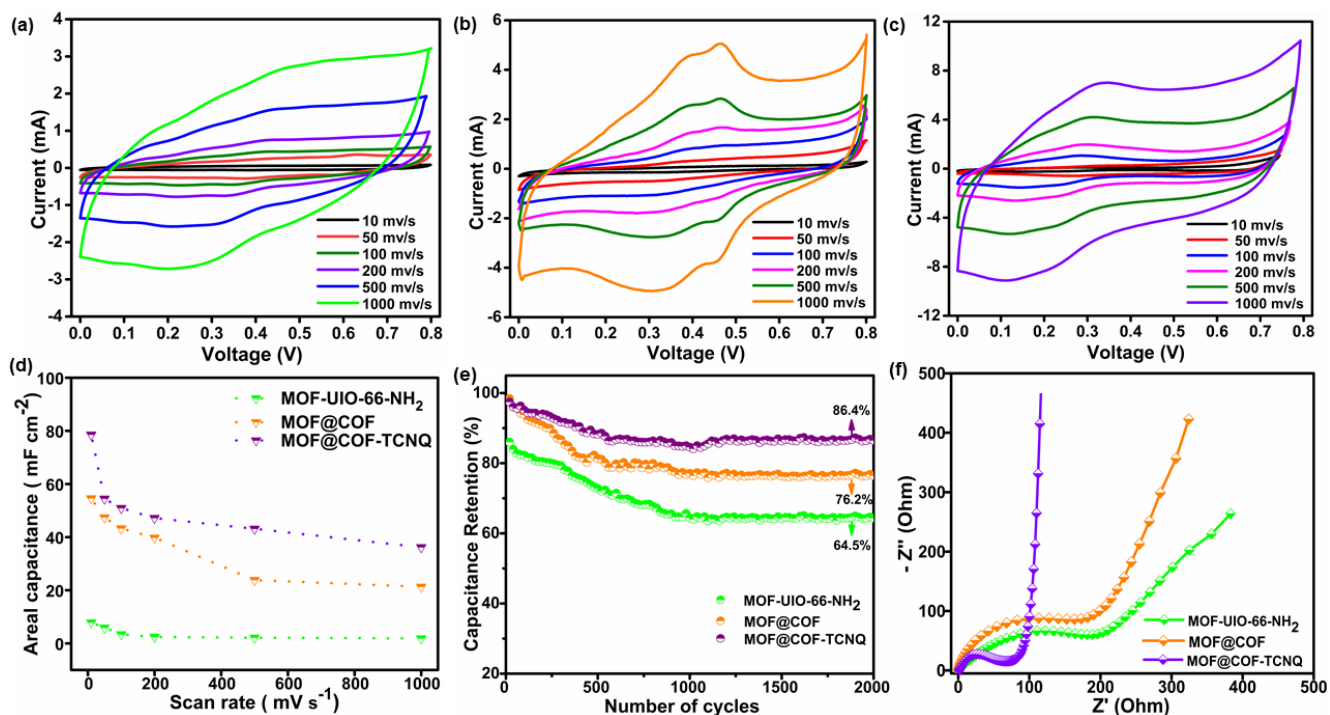


Figure 4. CV curves of a) MOF-UIO-66-NH₂, b) MOF@COF, c) MOF@COF-TCNQ, d) areal capacitance, e) capacitance retention, and f) Nyquist electrochemical impedance spectra.

Density Functional Theory (DFT) Calculations. In order to attain a greater understanding on the significant capacitance increase of MOF@COF after infiltration with TCNQ molecules, we performed DFT calculations and investigated the electronic properties and quantum capacitance, which is conducive to enhance the total electrochemical performances. As previously reported, the total capacity of the supercapacitors can be regarded as a series combination of double-layer capacitance and quantum capacitance when there is no consideration of pseudocapacitance. The quantum capacitance was calculated by considering the electronic structure of employed hybrids, *i.e.*, the DOS near the Fermi level.^{60,61} Therefore, we first built and optimized the models of MOF-UIO-66-NH₂ and COF-TpPa, then calculated their partial densities of states (PDOS) and local densities of states (LDOS), respectively (Figure S16-17). Based on PDOS and LDOS analyses of the MOF-UIO-66-NH₂ and COF-TpPa, we calculated the theoretical surface areas of the MOF-

UIO-66-NH₂ monolayer (Figure 5a and 5b). The heterostructure of MOF@COF was also built based on the MOF-UIO-66-NH₂ monolayer and COF-TpPa structure (Figure 5c-d). Further, we simulated the MOF@COF-TCNQ structure by adding the TCNQ molecules in the pores of COF-TpPa to simulate the TCNQ incorporated MOF@COF-TCNQ hybrid materials (Figure 5e and 5f).

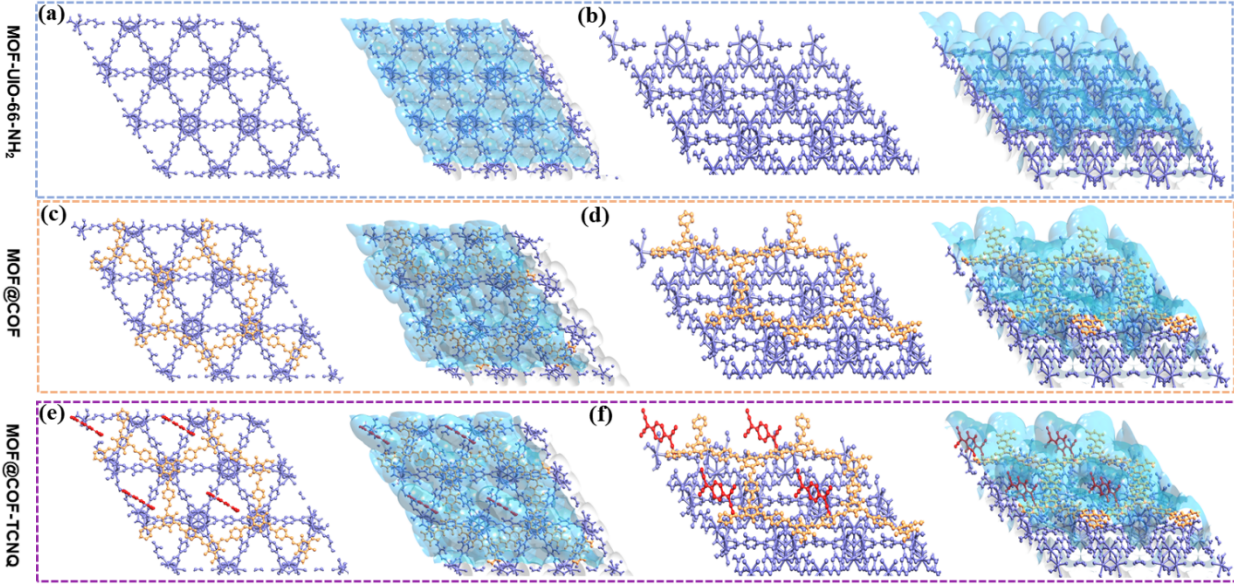


Figure 5. Top-view and side-view of model structures and iso-surfaces of (a-b) MOF-UIO-66-NH₂-monolayer structure; (c-d) MOF@COF structure; (e-f) MOF@COF-TCNQ structure. For clarity, H atoms are not displayed.

The DOS of MOF-UIO-66-NH₂-monolayer, MOF@COF heterostructure, and MOF@COF-TCNQ were investigated to calculate their quantum capacitance (Figure 6a). The quantum capacitance (C_Q) can be obtained from the density of states from the equation⁶²:

$$C_Q = \frac{e^2}{S/2} \int_{-\infty}^{+\infty} D(E) F_T(E - \mu) dE \quad (1)$$

where μ represents the electrochemical potential, $F_T(E)$ is the thermal broadening function $[(4kT)^{-1} \text{sech}^2(E/2kT)]$, $D(E)$ is the electron density of states, , in our case, $T = 300\text{K}$, E is the relative energy with respect to the Fermi level E_F , e is the elementary charge,⁶³ and S is the

calculated theoretical monolayer surface area (Table S2). The calculated quantum capacitance results demonstrate that MOF-UIO-66-NH₂-monolayer exhibits a highest value of 86 $\mu\text{F cm}^{-2}$ compared with COF-TpPa of 67 $\mu\text{F cm}^{-2}$. The quantum capacitance of the MOF@COF heterostructure resulted 26 $\mu\text{F cm}^{-2}$ lower than MOF-UIO-66-NH₂-monolayer. However, after doping the MOF@COF with TCNQ molecules (~ 5 wt%, to be consistent with the experiment results), the MOF@COF-TCNQ delivers obvious increased C_Q with a maximum value of 218 $\mu\text{F cm}^{-2}$ (Figure 6b).

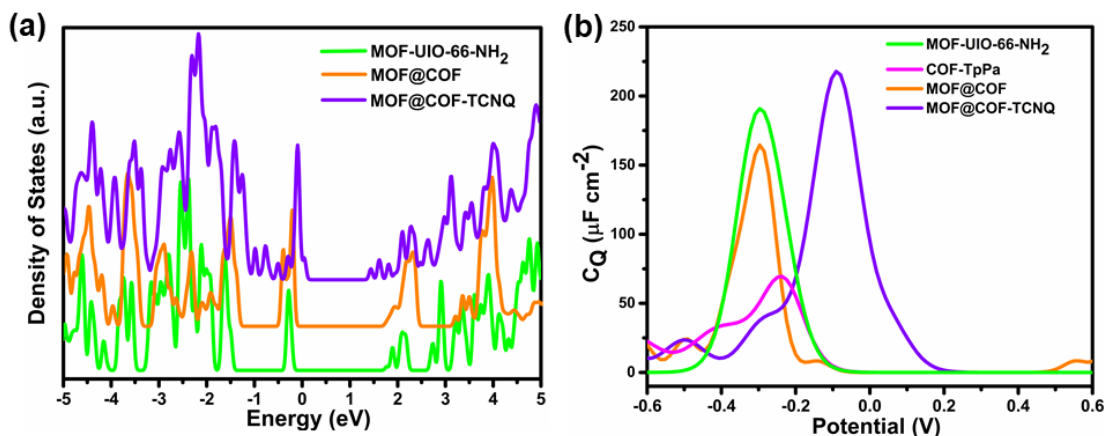


Figure 6. Calculated density of states (DOS) of (a) MOF-UIO-66-NH₂, (b) MOF@COF, (c) MOF@COF-TCNQ $\sim 5\%$. (d) Calculated potential-dependent quantum capacitances.

To further probe the effect of TCNQ content with C_Q on MOF@COF hybrid materials, we also explored the influence of different contents of TCNQ into MOF@COF heterostructure and calculated the DOS and C_Q for MOF@COF-TCNQ $\sim 1\%$ (Figure S18), MOF@COF-TCNQ $\sim 2\%$ (Figure S19), and MOF@COF-TCNQ $\sim 3\%$ (Figure S20). A strong correlation between the calculated C_Q and the TCNQ concentration was observed.

CONCLUSIONS

In conclusion, we have demonstrated a facile synthesis of a hybrid MOF@COF-TCNQ *via* liquid-phase infiltration of TCNQ molecules into the MOF@COF scaffold. This hybrid MOF@COF-TCNQ display a high specific areal capacitance of 78.36 mF cm⁻², and an excellent stack capacitance of 4.46 F cm⁻³, with capacitance retention of 86.4% after 2000 cycles, which outperforms the majority of the known MOFs@COFs hybrids. By combining experimental results with theoretical DFT calculations, MOF@COF-TCNQ outstanding performance has been attributed to the favorable synergistic effects of (i) the high crystallinity degree and the presence of uniform pores facilitating the diffusion of ions; (ii) the redox behavior of doped β -keto-enamine linked COF on MOF providing extra pseudocapacitance; and (iii) the infiltration of redox-active TCNQ molecules into MOF@COF hybrid frameworks endowing an enhanced electrical density of states (DOS) and quantum capacitance (CQ). Our strategy relying on post-synthetic modification of MOFs@COFs hybrids represents an effective route for future design of high-performance supercapacitor electrodes and provides an efficient strategy to increase the electrical DOS and CQ of MOF@COF hybrid materials.

EXPERIMENTAL SECTION

Synthesis of MOF-UIO-66-NH₂. 2-Aminoterephthalic acid (NH₂-BDC) (0.54 g, 3 mmol) and ZrCl₄ (0.5g, 2 mmol) were solubilized in 40 mL of DMF and sonicated for 30 minutes. Then, 1g PVP was added to the mixture and subsequently sonicated for 30 minutes. The mixed solution, which became transparent, was transferred into a 100 mL round-bottom flask for the hydrothermal treatment at 120°C for 24h. After cooling to room temperature, the resultant suspension was centrifuged and rinsed with DMF, acetone, and ethanol for three times, and then the product was activated with anhydrous acetone for 3 days and dried in a vacuum oven at 120°C for 12 h.

Synthesis of MOF@COF hybrid. The MOF@COF hybrid porous material was prepared by adding 60 mg of MOF-UIO-66-NH₂ powder and 16 mg of 1,3,5-triformylphloroglucinol to 4 ml of 1,4-dioxane solution. The mixture was sonicated for 30 min and heated at 80 °C for 2 h in an oil bath and vigorously stirred. Then, 0.5 ml of acetic acid (3 M) was gradually added to the suspension under stirring, during which the mixture solution became brighter. 2 mL of a 1,4-dioxane solution containing 16 mg *p*-phenylenediamine was dropped into the above suspension in 20 min and continued stirring for 1 h. The vial was then degassed through 3 freeze–pump–thaw cycles and the vial was sealed and heated at 120 °C for 3 days. The resulting product was collected at 40 °C by means of centrifugation and rinsed with acetone, tetrahydrofuran, and methanol, respectively, and desiccated under vacuum.

Synthesis of MOF@COF-TCNQ hybrid materials. The as-prepared MOF@COF powders have been infiltrated with TCNQ by thermal annealing under vacuum (150 °C for 2 h) to eliminate coordinated H₂O molecules, then instantly transfer to a TCNQ saturated solution in CH₂Cl₂. The infiltrated MOF@COF samples were then rinsed with EtOH and CH₂Cl₂ solvent to eliminate excess of non-infiltrated TCNQ, which might be physisorbed on the outer surface of MOF@COF powder. Furthermore, samples have been processed in ambient conditions, thus exposing the host-guest system to environmental amounts of solvent and moisture.

Material Characterization. The structure of all hybrid materials, as well as their composition were examined with various techniques. X-ray powder diffraction (XRD) patterns have been acquired with Bruker D8 X-ray diffractometer. Fourier transform infrared (FT-IR) spectra were recorded using the FT-IR 4700 Fourier Transform Infrared Spectrometer (JASCO)

equipped with ATR Diamond. Thermogravimetric analyses (TGA) curves have been acquired under N₂ atmosphere in the temperature range 25-800 °C, with a thermal step of 10 °C/min (SDTA851e system). Micromeritics ASAP 2050 analyzer was used to provide information on the specific surface area of investigated materials, which were degassed at 100 °C for 10h. FEI Quanta FEG 250 instrument S3 scanning electron microscope (SEM, FEI corporate, Hillsboro, Oregon, USA) was used for morphology analysis. Thermo Scientific K-Alpha X-ray photoelectron spectrometer bearing an aluminum X-ray source (energy 1.4866 keV) with X-ray beam spot fixed at 400 μm have been employed to provide detail on binding energies between the atoms in the samples. JEOL 2100 F transmission electron microscope operating at 200 kV, equipped with a Cs probe corrector and a GATAN Tridiem imaging filter was used. The material was drop-cast on a TEM grids covered by a lacey carbon membrane. MALDI-TOF mass spectrometry analysis was performed on a Bruker MicroflexLRF mass spectrometer in positive ions.

Electrochemical Measurements. Electrochemical performance analyses were investigated in both 2- and 3-electrode coin-type cells (CR2032) configurations. The slurry for both two- and three-electrode was fabricated in the same way according to the previously reported method.²⁴ Typically, dispersions of MOF-UIO-66-NH₂ (70.0mg) were obtained with 53 μL of oleic acid in 5.0 mL of hexane upon ultra-sonication for 3 h. Subsequently, the mixture was separated from 1.0 mL of dispersion by centrifugation (9000 rpm, 10 min), it was re-dispersed into 1.0 mL of a hexane solution containing 0.5 mg mL⁻¹ of graphene (3.3 wt.% relative to MOF-UIO-66-NH₂). For the three-electrode cell setup, the above dispersion solution was coated on stainless steel (1.5cm×1.5cm), Pt sheet, and saturated calomel electrode as the counter and reference electrodes, respectively. For the two-electrode cell setup, the above dispersion solution was coated on stainless

steel plates and drying at 80 °C under vacuum. Then the electrode was cut into several small slices (1.6 × 1.6 cm²) before assembling the cell. Two small slices were sandwiched with a separator (regenerated cellulose film, thickness 25 μm) in a coin-shaped cell and soaked with 1 M solution of tetraethylammonium tetrafluoroborate (TEABF₄) in acetonitrile. All electrochemical characterizations were executed with an Autolab PGSTAT128N Potentiostat/Galvanostat instruments with a Metrohm Autolab DuoCoin Cell Holder (Metrohm AG). The capacitance values of two-electrode were quantified upon fitting the electrical impedance spectroscopy (EIS) to an R(RC) equivalent circuit utilizing Nova 2.1 software (Eco Chemie) with an error below 1%. The 3-electrode based areal capacitance (F cm⁻²) was quantified from CV curves utilizing Formula 2, where I (A) was the response current, ΔV (V) corresponds to the voltage window, *v* (mV S⁻¹) is the scan rate and S (cm²) is the geometrical area of the electrode, stack capacitance was changed the S (cm²) to V (cm³), the volumetric of the electrode.

$$C = \frac{\int I dV}{v S \Delta V} \quad (2)$$

Computational methods. Density functional theory (DFT) calculations were carried out exploiting the Vienna *ab initio* package (VASP)⁶⁴ with the projector-augmented wave (PAW)⁶⁵ method. All calculations have been carried out employing the identical generalized gradient approximation (GGA) procedure with Perdew-Burke-Ernzerhof (PBE)⁶⁶ functional for the exchange-correlation term. The plane wave cutoff has been defined as 400 eV. The Brillouin zone integration was carried out with a 1×1×1 Monkhorst-Pack k-point grid in structure optimization and electronic properties simulations. The convergence of forces and energy were set to 0.01 eV Å⁻¹ and 5×10⁻⁵ eV, respectively.

ASSOCIATED CONTENT

*s1 Supporting Information. The Supporting Information is available free of charge at..

Supporting figures include XRD patterns, FT-IR spectra, XPS, MALDI-TOF mass spectra, TGA and DSC thermograms, BET pore-size distribution and surface area, charge/discharge curves, electrochemical kinetics study, Nyquist electrochemical impedance spectra, and DFT calculations details.

AUTHOR INFORMATION

Corresponding authors

*E-mail: ciesielski@unistra.fr

*E-mail : samori@unistra.fr

ORCID :

Haijun Peng: 0000-0002-8623-4339

Senhe Huang: 0000-0003-2352-1856

Diana Tranca: 0000-0001-9373-4975

Walid Baaziz: 0000-0002-3749-6105

Xiaodong Zhuang: 0000-0002-4090-0420

Artur Ciesielski: 0000-0003-3542-4092

Paolo Samorì: 0000-0001-6256-8281

Author Contributions

H.P. and A.C. conceived and designed the project. H.P. performed the synthesis and characterization of obtained MOF-based materials as well as the supercapacitor fabrication and evaluation. S.H., D.T., and X.Z. performed the DFT calculations. F.R. performed the XPS study. W.B. performed the high-resolution TEM measurements. All authors discussed the results and contributed to the interpretation of data. H.P., P.S., and A.C. co-wrote the paper with input from all co-authors.

Notes

The authors declare no competing financial interest.

ACKNOWLEDGMENT

Dr. Cataldo Valentini and Dr. Iwona Janica are acknowledged for the help of MALDI-TOF mass spectra and PXRD measurements. We acknowledge the financial support from the European Commission through the Marie Skłodowska-Curie project ULTIMATE (GA-813036), the Agence Nationale de la Recherche through the Labex project CSC (ANR-10-LABX-0026 CSC) within the Investissement d'Avenir program (ANR-10-120 IDEX-0002-02), the International Center for Frontier Research in Chemistry (icFRC), the Polish National Science Center (Grant No. 2019/35/B/ST5/01568), the Institut Universitaire de France (IUF) and the Chinese Scholarship Council.

REFERENCES

1. Simon, P.; Gogotsi, Y. Materials for Electrochemical Capacitors. *Nat. Mater.* **2008**, *7*, 845-854.

2. Wang, F.; Wu, X.; Yuan, X.; Liu, Z.; Zhang, Y.; Fu, L.; Zhu, Y.; Zhou, Q.; Wu, Y.; Huang, W. Latest Advances in Supercapacitors: From New Electrode Materials to Novel Device Designs. *Chem. Soc. Rev.* **2017**, *46*, 6816-6854.
3. Li, K.; Wang, X.; Wang, X.; Liang, M.; Nicolosi, V.; Xu, Y.; Gogotsi, Y. All-Pseudocapacitive Asymmetric MXene-Carbon-Conducting Polymer Supercapacitors. *Nano Energy* **2020**, *75*, 104971.
4. Tang, J.; Mathis, T.; Zhong, X.; Xiao, X.; Wang, H.; Anayee, M.; Pan, F.; Xu, B.; Gogotsi, Y. Optimizing Ion Pathway in Titanium Carbide MXene for Practical High-Rate Supercapacitor. *Adv. Energy Mater.* **2021**, *11*, 2003025.
5. Gogotsi, Y. Energy Storage Wrapped Up. *Nature* 2014, *509*, 568-569.
6. Alhokbany, N.; Ahmed, J.; Ubaidullah, M.; Mutehri, S.; Khan, M. A. -M.; Ahamad, T.; Alshehri, S. -M. Cost-Effective Synthesis of NiCo₂O₄@Nitrogen-Doped Carbon Nanocomposite Using Waste PET Plastics for High-Performance Supercapacitor. *J. Mater. Sci.: Mater. Electron.* **2020**, *31*, 16701-16707.
7. Ubaidullah, M.; Al-Enizi, A. -M.; Ahamad, T.; Shaikh, S. F.; Al-Abdrabalnabi, M. -A.; Samdani, M. -S.; Kumar, D.; Alam, M. -A.; Khan, M. Fabrication of Highly Porous N-Doped Mesoporous Carbon Using Waste Polyethylene Terephthalate Bottle-Based MOF-5 for High Performance Supercapacitor. *J. Energy Storage* **2021**, *33*, 102125.
8. El-Gendy, D. -M.; Abdel Hameed, R. -M.; Al-Enizi, A. -M.; Bakrey, M.; Ubaidullah, M.; Yousef, A., Synthesis and Characterization of WC@GNFs as an Efficient Supercapacitor Electrode Material in Acidic Medium. *Ceram. Int.* **2020**, *46*, 27437-27445.

9. Xia, J.; Chen, F.; Li, J.; Tao, N. Measurement of the Quantum Capacitance of Graphene. *Nat. Nanotechnol.* **2009**, *4*, 505-509.
10. Ilani, S.; Donev, L. A. K.; Kindermann, M.; McEuen, P. L. Measurement of the Quantum Capacitance of Interacting Electrons in Carbon Nanotubes. *Nat. Phys.* **2006**, *2*, 687-691.
11. Zhang, L. L.; Zhao, X.; Ji, H.; Stoller, M. D.; Lai, L.; Murali, S.; McDonnell, S.; Cleveger, B.; Wallace, R. M.; Ruoff, R. S. Nitrogen Doping of Graphene and Its Effect on Quantum Capacitance, and a New Insight on the Enhanced Capacitance of N-Doped Carbon. *Energy Environ. Sci.* **2012**, *5*, 9618-9625.
12. Song, C.; Wang, J.; Meng, Z.; Hu, F.; Jian, X. Density Functional Theory Calculations of the Quantum Capacitance of Graphene Oxide as a Supercapacitor Electrode. *Chemphyschem* **2018**, *19*, 1579-1583.
13. Zhou, H.; Long, J.; Yagi, O. Introduction to Metal–Organic Frameworks. *Chem. Rev.* **2012**, *112*, 673-674.
14. Geng, K.; He, T.; Liu, R.; Dalapati, S.; Tan, K. T.; Li, Z.; Tao, S.; Gong, Y.; Jiang, Q.; Jiang, D. Covalent Organic Frameworks: Design, Synthesis, and Functions. *Chem. Rev.* **2020**, *120*, 8814-8933.
15. Wang, M.; Guo, H.; Xue, R.; Li, Q.; Liu, H.; Wu, N.; Yao, W.; Yang, W. Covalent Organic Frameworks: A New Class of Porous Organic Frameworks for Supercapacitor Electrodes. *ChemElectroChem* **2019**, *6*, 2984-2997.
16. Al-Enizi, A. -M.; Ahmed, J.; Ubaidullah, M.; Shaikh, S. -F.; Ahamad, T.; Naushad, M.; Zheng, G. Utilization of Waste Polyethylene Terephthalate Bottles to Develop Metal-Organic

Frameworks for Energy Applications: A Clean and Feasible Approach. *J. Clean. Prod.* **2020**, *248*, 119251.

17. Ubaidullah, M.; Al-Enizi, A. -M.; Shaikh, S.; Ghanem, M. -A.; Mane, R. -S. Waste PET Plastic Derived ZnO@NMC Nanocomposite *via* MOF-5 Construction for Hydrogen and Oxygen Evolution Reactions. *J. King Saud Univ. Sci.* **2020**, *32*, 2397-2405.

18. Hong, X.-J.; Song, C.-L.; Yang, Y.; Tan, H.-C.; Li, G.-H.; Cai, Y.-P.; Wang, H. Cerium Based Metal–Organic Frameworks as an Efficient Separator Coating Catalyzing the Conversion of Polysulfides for High Performance Lithium–Sulfur Batteries. *ACS Nano* **2019**, *13*, 1923-1931.

19. Yang, Y.; Hong, X.-J.; Song, C.-L.; Li, G.-H.; Zheng, Y.-X.; Zhou, D.-D.; Zhang, M.; Cai, Y.-P.; Wang, H., Lithium Bis(trifluoromethanesulfonyl)imide Assisted Dual-Functional Separator Coating Materials Based on Covalent Organic Frameworks for High-Performance Lithium–Selenium Sulfide Batteries. *J. Mater. Chem. A* **2019**, *7*, 16323-16329.

20. Hong, X.-J.; Song, C.-L.; Wu, Z.-M.; Li, Z.-H.; Cai, Y.-P.; Wang, C.-X.; Wang, H. Sulfophilic and Lithophilic Sites in Bimetal Nickel-Zinc Carbide with Fast Conversion of Polysulfides for High-Rate Li-S Battery. *Chem. Eng. J.* **2021**, *404*, 126566.

21. Talin, A. A.; Centrone, A.; Ford, A. C.; Foster, M. E.; Stavila, V.; Haney, P.; Kinney, R. A.; Szalai, V.; El Gabaly, F.; Yoon, H. -P.; Léonard, F.; Allendorf, M. -D. Tunable Electrical Conductivity in Metal-Organic Framework Thin-Film Devices. *Science* **2014**, *343*, 66.

22. Li, J.; Jing, X.; Li, Q.; Li, S.; Gao, X.; Feng, X.; Wang, B. Bulk COFs and COF Nanosheets for Electrochemical Energy Storage and Conversion. *Chem. Soc. Rev.* **2020**, *49*, 3565-3604.

23. Petit, C.; Bandosz, T. -J. MOF–Graphite Oxide Composites: Combining the Uniqueness of Graphene Layers and Metal–Organic Frameworks. *Adv. Mater.* **2009**, *21*, 4753-4757.
24. Choi, K. -M.; Jeong, H. -M.; Park, J. -H.; Zhang, Y.-B.; Kang, J. -K.; Yaghi, O. -M. Supercapacitors of Nanocrystalline Metal–Organic Frameworks. *ACS Nano* **2014**, *8*, 7451-7457.
25. Lu, C.; Ben, T.; Xu, S.; Qiu, S. Electrochemical Synthesis of a Microporous Conductive Polymer Based on a Metal–Organic Framework Thin Film. *Angew. Chem. Int. Ed.* **2014**, *53*, 6454-6458.
26. Kalaj, M.; Bentz, K. -C.; Ayala, S.; Palomba, J. -M.; Barcus, K. -S.; Katayama, Y.; Cohen, S. -M. MOF-Polymer Hybrid Materials: From Simple Composites to Tailored Architectures. *Chem. Rev.* **2020**, *120*, 8267-8302.
27. Fu, J.; Das, S.; Xing, G.; Ben, T.; Valtchev, V.; Qiu, S. Fabrication of COF-MOF Composite Membranes and Their Highly Selective Separation of H₂CO₂. *J. Am. Chem. Soc.* **2016**, *138*, 7673-7680.
28. Zhang, F.-M.; Sheng, J.-L.; Yang, Z.-D.; Sun, X.-J.; Tang, H.-L.; Lu, M.; Dong, H.; Shen, F.-C.; Liu, J.; Lan, Y.-Q. Rational Design of MOF/COF Hybrid Materials for Photocatalytic H₂ Evolution in the Presence of Sacrificial Electron Donors. *Angew. Chem. Int. Ed.* **2018**, *57*, 12106-12110.
29. Sun, D.; Jang, S.; Yim, S.-J.; Ye, L.; Kim, D.-P. Metal Doped Core–Shell Metal-Organic Frameworks@Covalent Organic Frameworks (MOFs@COFs) Hybrids as a Novel Photocatalytic Platform. *Adv. Fun. Mater.* **2018**, *28*, 1707110.

30. Zhou, N.; Ma, Y.; Hu, B.; He, L.; Wang, S.; Zhang, Z.; Lu, S. Construction of Ce-MOF@COF Hybrid Nanostructure: Label-Free Aptasensor for the Ultrasensitive Detection of Oxytetracycline Residues in Aqueous Solution Environments. *Biosens. Bioelectron.* **2019**, *127*, 92-100.
31. Zhang, L.; Liu, Z.; Deng, Q.; Sang, Y.; Dong, K.; Ren, J.; Qu, X. Nature-Inspired Construction of MOF@COF Nanozyme with Active Sites in Tailored Microenvironment and Pseudopodia-Like Surface for Enhanced Bacterial Inhibition. *Angew. Chem. Int. Ed.* **2021**, *60*, 3469-3474.
32. Sun, W.; Tang, X.; Yang, Q.; Xu, Y.; Wu, F.; Guo, S.; Zhang, Y.; Wu, M.; Wang, Y. Coordination-Induced Interlinked Covalent and Metal-Organic-Framework Hybrids for Enhanced Lithium Storage. *Adv. Mater.* **2019**, *31*, 1903176.
33. Peng, Y.; Zhao, M.; Chen, B.; Zhang, Z.; Huang, Y.; Dai, F.; Lai, Z.; Cui, X.; Tan, C.; Zhang, H. Hybridization of MOFs and COFs: A New Strategy for Construction of MOF@COF Core-Shell Hybrid Materials. *Adv. Mater.* **2018**, *30*, 1705454.
34. Schneider, C.; Ukaj, D.; Koerver, R.; Talin, A. -A.; Kieslich, G.; Pujari, S. -P.; Zuilhof, H.; Janek, J.; Allendorf, M. -D.; Fischer, R. -A. High Electrical Conductivity and High Porosity in a Guest@MOF Material: Evidence of TCNQ Ordering within Cu₃BTC₂ Micropores. *Chem. Sci.* **2018**, *9*, 7405-7412.
35. Usov, P. -M.; Jiang, H.; Chevreau, H.; Peterson, V. -K.; Leong, C. -F.; D'Alessandro, D.-M. Guest-Host Complexes of TCNQ and TCNE with Cu₃(1,3,5-Benzenetricarboxylate)₂. *J. Phys. Chem. C* **2017**, *121*, 26330-26339.

36. Nie, X.; Kulkarni, A.; Sholl, D. S. Computational Prediction of Metal Organic Frameworks Suitable for Molecular Infiltration as a Route to Development of Conductive Materials. *J. Phys. Chem. Lett.* **2015**, *6*, 1586-1591.
37. Bláha, M.; Valeš, V.; Bastl, Z.; Kalbáč, M.; Shiozawa, H. Host–Guest Interactions in Metal–Organic Frameworks Doped with Acceptor Molecules as Revealed by Resonance Raman Spectroscopy. *J. Phys. Chem. C* **2020**, *124*, 24245-24250.
38. Leith, G. -A.; Rice, A. -M.; Yarbrough, B. -J.; Berseneva, A. -A.; Ly, R. -T.; Buck Iii, C. -N.; Chusov, D.; Brandt, A. -J.; Chen, D. -A.; Lamm, B. -W.; Stefik, M.; Stephenson, K. -S.; Smith, M. -D.; Vannucci, A. -K.; Pellechia, P. -J.; Garashchuk, S.; Shustova, N.- B. A Dual Threat: Redox-Activity and Electronic Structures of Well-Defined Donor–Acceptor Fulleretic Covalent-Organic Materials. *Angew. Chem. Int. Ed.* **2020**, *59*, 6000-6006.
39. He, Y.; Yang, S.; Fu, Y.; Wang, F.; Ma, J.; Wang, G.; Chen, G.; Wang, M.; Dong, R.; Zhang, P.; Feng, X. Electronic Doping of Metal-Organic Frameworks for High-Performance Flexible Micro-Supercapacitors. *Small Struct.* **2020**, *2*, 2000095.
40. Gomes Silva, -C.; Luz, I.; Llabrés i Xamena, F. -X.; Corma, A.; García, H. Water Stable Zr–Benzenedicarboxylate Metal–Organic Frameworks as Photocatalysts for Hydrogen Generation. *Chem. Eur. J.* **2010**, *16*, 11133-11138.
41. Kandambeth, S.; Mallick, A.; Lukose, B.; Mane, M. V.; Heine, T.; Banerjee, R. Construction of Crystalline 2D Covalent Organic Frameworks with Remarkable Chemical (Acid/Base) Stability via a Combined Reversible and Irreversible Route. *J. Am. Chem. Soc.* **2012**, *134*, 19524-19527.

42. DeBlase, C. -R.; Silberstein, K. -E.; Truong, T.-T.; Abruña, H. -D.; Dichtel, W. -R. β -Ketoenamine-Linked Covalent Organic Frameworks Capable of Pseudocapacitive Energy Storage. *J. Am. Chem. Soc.* **2013**, *135*, 16821-16824.
43. Halder, A.; Ghosh, M.; Khayum M, -A.; Bera, S.; Addicoat, M.; Sasmal, H. -S.; Karak, S.; Kurungot, S.; Banerjee, R. Interlayer Hydrogen-Bonded Covalent Organic Frameworks as High-Performance Supercapacitors. *J. Am. Chem. Soc.* **2018**, *140*, 10941-10945.
44. Yusran, Y.; Fang, Q.; Valtchev, V. Electroactive Covalent Organic Frameworks: Design, Synthesis, and Applications. *Adv. Mater.* **2020**, *32*, 2002038.
45. Sun, T.; Xie, J.; Guo, W.; Li, D.-S.; Zhang, Q. Covalent–Organic Frameworks: Advanced Organic Electrode Materials for Rechargeable Batteries. *Adv. Energy Mater.* **2020**, *10*, 1904199.
46. Pal, S.; Maiti, S.; Maiti, U. -N.; Chattopadhyay, K. -K. Scalable Approach for the Realization of Garland Shaped 3D Assembly of CuTCNQ Nanorods: An Efficient Electron Emitter. *J. Mater. Chem. C* **2014**, *2*, 4005-4011.
47. Jin, E.; Asada, M.; Xu, Q.; Dalapati, S.; Addicoat, M. -A.; Brady, M. -A.; Xu, H.; Nakamura, T.; Heine, T.; Chen, Q.; Jiang, D. Two-Dimensional Sp² Carbon–Conjugated Covalent Organic Frameworks. *Science* **2017**, *357*, 673.
48. Xu, J.; He, S.; Zhang, H.; Huang, J.; Lin, H.; Wang, X.; Long, J. Layered Metal–Organic Framework/Graphene Nanoarchitectures for Organic Photosynthesis under Visible Light. *J. Mater. Chem. A* **2015**, *3*, 24261-24271.
49. Yao, Y.-H.; Li, J.; Zhang, H.; Tang, H.-L.; Fang, L.; Niu, G.-D.; Sun, X.-J.; Zhang, F.-M. Facile Synthesis of a Covalently Connected rGO–COF Hybrid Material by *in Situ* Reaction for

Enhanced Visible-Light Induced Photocatalytic H₂ Evolution. *J. Mater. Chem. A* **2020**, *8*, 8949-8956.

50. Capitán, M. J.; Álvarez, J.; Navio, C. Study of the Electronic Structure of Electron Accepting Cyano-Films: TCNQ *versus* TCNE. *Phys. Chem. Chem. Phys.* **2018**, *20*, 10450-10459.

51. Son, S.-B.; Gao, T.; Harvey, S. P.; Steirer, K. X.; Stokes, A.; Norman, A.; Wang, C.; Cresce, A.; Xu, K.; Ban, C. An Artificial Interphase Enables Reversible Magnesium Chemistry in Carbonate Electrolytes. *Nat. Chem.* **2018**, *10*, 532-539.

52. Bonnet, S.; Forano, C.; Besse, J.-P. Intercalation of Tetracyanoquinodimethane in [Zn–Al] Layered Double Hydroxide. *Mater. Res. Bull.* **1998**, *33*, 783-788.

53. Ubaidullah, M.; Ahmed, J.; Ahamad, T.; Shaikh, S. -F.; Alshehri, S. -M.; Al-Enizi, A. -M. Hydrothermal Synthesis of Novel Nickel Oxide@Nitrogenous Mesoporous Carbon Nanocomposite Using Costless Smoked Cigarette Filter for High Performance Supercapacitor. *Mater. Lett.* **2020**, *266*, 127492.

54. Gogotsi, Y.; Simon, P. True Performance Metrics in Electrochemical Energy Storage. *Science* **2011**, *334*, 917.

55. Xu, F.; Xu, H.; Chen, X.; Wu, D.; Wu, Y.; Liu, H.; Gu, C.; Fu, R.; Jiang, D. Radical Covalent Organic Frameworks: A General Strategy to Immobilize Open-Accessible Polyradicals for High-Performance Capacitive Energy Storage. *Angew. Chem. Int. Ed.* **2015**, *54*, 6814-6818.

56. Raymundo-Piñero, E.; Cadek, M.; Béguin, F. Tuning Carbon Materials for Supercapacitors by Direct Pyrolysis of Seaweeds. *Adv. Fun. Mater.* **2009**, *19*, 1032-1039.

57. Kou, Y.; Xu, Y.; Guo, Z.; Jiang, D. Supercapacitive Energy Storage and Electric Power Supply Using an Aza-Fused π -Conjugated Microporous Framework. *Angew. Chem. Int. Ed.* **2011**, *50*, 8753-8757.
58. Wu, X.; Hong, J. J.; Shin, W.; Ma, L.; Liu, T.; Bi, X.; Yuan, Y.; Qi, Y.; Surta, T. W.; Huang, W.; Neufeind, J.; Wu, T.; Greaney, P. A.; Lu, J.; Ji, X. Diffusion-Free Grotthuss Topochemistry for High-Rate and Long-Life Proton Batteries. *Nat. Energy* **2019**, *4*, 123-130.
59. Zhang, S.; Pan, N. Supercapacitors Performance Evaluation. *Adv. Energy Mater.* **2015**, *5*, 1401401.
60. Zhan, C.; Lian, C.; Zhang, Y.; Thompson, M. W.; Xie, Y.; Wu, J.; Kent, P. R. -C.; Cummings, P. -T.; Jiang, D.-E.; Wesolowski, D. -J. Computational Insights into Materials and Interfaces for Capacitive Energy Storage. *Adv. Sci.* **2017**, *4*, 1700059.
61. Mousavi-Khoshdel, M.; Targholi, E.; Momeni, M. -J. First-Principles Calculation of Quantum Capacitance of Codoped Graphenes as Supercapacitor Electrodes. *J. Phys. Chem. C* **2015**, *119*, 26290-26295.
62. Paek, E.; Pak, A.-J.; Hwang, G.-S. A Computational Study of the Interfacial Structure and Capacitance of Graphene in [BMIM][PF₆] Ionic Liquid. *J. Electrochem. Soc.* **2012**, *160*, A1-A10.
63. Paek, E.; Pak, A.-J.; Kweon, K.-E.; Hwang, G.-S. On the Origin of the Enhanced Supercapacitor Performance of Nitrogen-Doped Graphene. *J. Phys. Chem. C* **2013**, *117*, 5610-5616.
64. Kresse, G.; Furthmüller, J. Efficient Iterative Schemes for *ab Initio* Total-Energy Calculations Using a Plane-Wave Basis Set. *Phys. Rev. B* **1996**, *54*, 11169-11186.

65. Blöchl, P. -E. Projector Augmented-Wave Method. *Phys. Rev. B* **1994**, *50*, 17953-17979.
66. Perdew, J.-P.; Burke, K.; Ernzerhof, M. Generalized Gradient Approximation Made Simple. *Phys. Rev. Lett.* **1996**, *77*, 3865-3868.